Title
Double-couple earthquake focal mechanism: random rotation and display

Journal
Geophysical Journal International, 163(3)

ISSN
0956-540X

Author
Kagan, Yan Y

Publication Date
2005-12-01

Double-couple earthquake focal mechanism: Random rotation and display

Yan Y. Kagan[1]

[1] Department of Earth and Space Sciences, University of California, Los Angeles, California, USA

Abstract. This paper addresses two problems: the random rotation of double-couple (DC) earthquake sources and the display of earthquake focal mechanisms. We consider several equivalent representations for DC sources and their properties and provide mathematical expressions for their mutual transformation. Obviously, a 3-D rotation of any object is more intricate than a 2-D rotation. Any rotation of a DC source is further complicated by its symmetry properties. Applying statistical tests to a DC distribution often requires one to compare it to a completely (or uniform) random DC pattern. We review several methods for obtaining random distribution of DC orientation; some of these seemingly natural techniques yield an incorrect result.

The DC random rotation problem is closely connected to displays of focal mechanisms. In such displays, a strike or an azimuth of a focal mechanism can be neglected; hence, we are confronted with mapping a two-dimensional distribution onto a flat surface. We review different methods for such displays and discuss more specifically how to project a random focal mechanism distribution on a flat 2-D display with uniform probability density. Such displays can be used to analyze earthquake patterns statistically in various tectonic regions.

INDEX TERMS: Seismology (ESE): 7215 Earthquake parameters; 7209 Earthquake dynamics and mechanics;

KEYWORDS: Earthquake focal mechanisms, their representations, double-couples, random rotation, focal mechanism displays

KEYWORDS: Earthquake-source mechanism, Fault-plane solutions, Seismic moment, Seismotectonics, Statistical methods

1. Introduction

In this paper we discuss various mathematical representations for the double-couple (DC) earthquake focal mechanism, algorithms for DC random rotation and several methods to display DC sources. Recently there has been an increased interest in 3-D random rotation of earthquake focal mechanisms. Results of rotation simulation are being used in statistical tests of accuracy in determining earthquake source (Hardebeck & Shearer, 2002) or in studying how static stress triggers earthquakes (Steacy *et al.*, 2004).

The 3-D rotation, however, exhibits some complicated, counter-intuitive properties. Kendall & Moran (1963, Chapter 4.25) show that rotating an object around an axis selected uniformly from all possible axes in space and using a uniformly distributed angle yields no truly (or uniform) random 3-D rotation. They propose several methods for representation of 3-D rotation. Therefore, a 3-D rotation simulation requires more substantial analysis and testing. The results of such testing will help us propose and investigate new methods for displaying earthquake focal mechanisms. Such displays may be useful in studying complicated deformation patterns in earthquake zones. Moreover, increased availability of focal mechanism data in the Harvard CMT (Ekström *et al.*, 2005, and references therein) and other catalogues makes such investigation essential.

Among the methods for DC description we discuss the quaternion, eigenvector, and geologic/tectonic representations. Though mathematically equivalent, each of these methods, depending on their application, has certain advantages and disadvantages. Quaternions are especially useful in describing and simulating the 3-D rotation (Sections 3.1 and 3.4).

In this paper we commonly use the term 'DC source' to describe an arbitrarily oriented earthquake source, requiring at least three parameters for its full characterization. If the azimuthal source orientation is neglected, the 'focal mechanism' parameterization has two degrees of freedom.

2. DC representations

Several equivalent mathematical parameterizations are used to describe the DC earthquake source: eigenvectors or principal axes (T-, B-, and P-axes), geologic (fault/rupture plane and auxiliary plane, or nodal planes), normalized quaternion (Kagan & Knopoff, 1985; Kagan, 1991; Ward, 1997; Kuipers, 2002), and normalized seismic moment tensor. Of these, quaternions are least known to earth scientists, although, for example, Le Pichon *et al.* (1973, p. 38) state that the quaternion representation of 3-D rotations "... provide[s] a most concise development." Other representations of finite 3-D rotations are less computationally convenient, especially if the sequence of rotations or an inverse rotation problem is considered (Kuipers, 2002). Three degrees of freedom are sufficient to fully describe a DC source orientation.

A standard display of a DC source employs a lower hemisphere stereographic or equal-area projection (Aki & Richards, 2002, their Figs. 4.16 and 4.17). Such plots are commonly called 'beachball' projections. However, earthquakes are often clustered in space, making beachball plots too complex to display and interpret. Although such spatial, temporal, and DC source distributions can be studied

either by descriptive characterization or more formal statistical techniques (Kagan, 1992a;b; 2001), the results of such investigations are difficult to visualize and evaluate. In addition, one may be interested not in the earthquake's position and distribution of DC sources, but instead the distribution of different focal mechanisms and their inter-relation. For such purposes the displays of mechanisms and their statistical analysis may be more advantageous.

2.1. Eigenvector representation

Three orthogonal axes T, P, and B describe the radiation of P-waves from a point DC source (Frohlich, 1996). They are eigenvectors of the seismic moment tensor. Since the tensor is symmetric, the direction of vectors can be selected arbitrarily; traditionally the axes are directed only downwards. Each is parameterized by two angles, plunge α and azimuth β. Since the DC source is defined by 3 degrees of freedom, 3 of these angles can be calculated if the other three are known.

We also categorize earthquakes according to their prevalent focal mechanism: *thrust*, *strike-slip*, and *normal*. For example, an earthquake is considered to have a normal focal mechanism if its most-compressive principal axis of the moment tensor (P-axis) is more vertical than either principal axis B or T (Frohlich 1992; 2001). Similarly, we define earthquakes with the thrust and strike-slip mechanism when the T-axis or B-axis is more vertical than the other axes, respectively.

2.2. Geologic/tectonic fault representation

Aki & Richards (2002), Jost & Herrmann (1989), Pujol & Herrmann (1990) and Dziewonski & Woodhouse (1983) discuss representing earthquake faults and connecting geometric fault plane parameters with the seismic moment tensor properties. The standard parameterization of a fault rupture plane involves defining its strike (azimuth) ϕ, dip δ, and rake λ. The plane orthogonal to the fault plane and slip vector is an auxiliary nodal plane. It is usually impossible to distinguish between these planes on the basis of far-field seismic radiation: this effect is known as the *ambiguity* of earthquake nodal planes. The nodal planes are usually arranged so that their dips $\delta_2 \geq \delta_1$.

The other nodal plane parameters can be obtained from the first plane by the following relations (cf. Ben-Menahem & Singh, 1981, p. 190):

$$\delta_2 \;=\; \arccos[\sin\delta_1 \, \sin\lambda_1] \,, \tag{1}$$

$$\lambda_2 \;=\; \arctan \frac{\cos\delta_1 / \sin\delta_2}{-\sin\delta_1 \, \cos\lambda_1 / \sin\delta_2} \,, \tag{2}$$

and

$$\phi_1 - \phi_2 \;=\; \arctan \frac{\cos\lambda_1 / \sin\delta_2}{-1/(\tan\delta_1 \, \tan\delta_2)} \,. \tag{3}$$

In (2) and (3) we do not cancel similar terms from the nominator and the denominator; these terms are needed when estimating the function arctan (ATAN2) in FORTRAN. If $\lambda_1 < 0^\circ$, $\delta_2' = 180^\circ - \delta_2$, $\lambda_2' = -\lambda_2$, and $(\phi_1 - \phi_2)' \;=\; \phi_2 - \phi_1$.

2.3. Quaternion representation

Kagan (1982) presented the orientation of a DC source by a normalized quaternion. The normalized quaternion $\mathbf{q} = [q_1, q_2, q_3, q_4]$ contains four terms which can be interpreted as defining a 3-D sphere in 4-D space:

$$q_1^2 + q_2^2 + q_3^2 + q_4^2 = 1 \,. \tag{4}$$

Hence the total number of degrees of freedom is 3. The normalized quaternion can be used to describe a 3-D rotation: in this case the first three terms in (4) characterize the direction of the rotation axis, and the fourth term stands for the angle of rotation (Kagan, 1991).

When applied to DC parametrization, the identity quaternion (zero rotation)

$$\mathbf{I} = [0, 0, 0, 1] \,, \tag{5}$$

is identified with the strike-slip DC source having plunge angles

$$\alpha_T = \alpha_P = 0^\circ, \quad \text{and} \quad \alpha_B = 90^\circ \,, \tag{6}$$

and azimuths

$$\beta_T = 0^\circ, \quad \text{and} \quad \beta_P = 90^\circ \,, \tag{7}$$

(Kagan, 1991). Any other DC source corresponds to a quaternion describing 3-D rotation from the reference source (Eqs. 5–7).

The FORTRAN programme which determines the 3-D rotation of DC sources is available on the Web – ftp://minotaur.ess.ucla.edu/pub/kagan/dcrot.for (see also FORTRAN90 adaptation of the programme by P. Bird ftp://element.ess.ucla.edu/2003107-esupp/Quaternion.f90). Frohlich & Davis (1999) also discuss the programme.

3-D rotations for quaternions of opposite signs are equal

$$\mathbf{q} \;=\; -\mathbf{q} \,. \tag{8}$$

Given the symmetry of the DC source (Kagan & Knopoff, 1985; Kagan, 1990; 1991) the q_4 term in (4) can always be presented as the largest positive term in this parameterization. In particular, to obtain the standard DC quaternion representation, we right-multiply an arbitrary normalized quaternion $\mathbf{q}$ by one of the elementary quaternions (Kagan, 1991):

$$\begin{aligned} &\mathbf{i} = [1, 0, 0, 0] \,; \\ &\mathbf{j} = [0, 1, 0, 0] \,; \\ &\mathbf{k} = [0, 0, 1, 0] \,, \end{aligned} \tag{9}$$

if the first, second, or third term has the largest absolute value, respectively. For example, for the largest first term

$$\mathbf{q}_2 \;=\; \mathbf{q}_1 \, \mathbf{i} \,. \tag{10}$$

If the resulting fourth term is negative, the sign of all terms should be reversed (see 8).

Thus, in our representation, an arbitrary quaternion is both a rotation operator and after simple transformations (8–10) is a DC source. Although the quaternion does not have the advantage of a clearly identifying the DC source properties, its benefits are obvious. Multiple rotations of the DC source as well as the inverse problem determining the rotation from one source to another are easily computed using methods of quaternion algebra (Kagan, 1991; Ward, 1997; Kuipers, 2002).

2.4. Seismic moment tensor representation

The seismic moment tensor is commonly represented as a symmetric second-order matrix. Formally it has 6 degrees of freedom, but the DC source corresponds to the normalized trace-free tensor with the zero determinant, so the total number of free parameters is 3.

Many textbooks show how to calculate the moment tensor for known faults or eigenvector parameters (see, for example, Aki & Richards, 2002). Kagan & Jackson (1994) propose formulae for calculating the seismic moment tensor for a known quaternion DC representation.

3. Random DC rotation

3.1. 3-D rotation angle distribution

Kagan (1990; 1992b) derived the distribution of the rotation angle Φ for a uniform random rotation of the DC source. That is, he demonstrated that a rotation of $2\pi/3$ or less about some axis is adequate to generate any double couple from any other double couple. He derived the distribution of the smallest such angle for pairs of double couples selected randomly from the distribution of all possible double couples. The p.d.f. is

$$f(\Phi) \;=\; (4/\pi)(1-\cos\Phi) \quad \text{for} \quad 0 \le \Phi \le \pi/2; \quad (11)$$

$$f(\Phi) \;=\; (4/\pi)(3\sin\Phi + 2\cos\Phi - 2) \quad \text{for} \quad \pi/2 \le \Phi \le \Phi_S; \quad (12)$$

and

$$f(\Phi) \;=\; (4/\pi)\Bigg\{3\sin\Phi + 2\cos\Phi - 2 - (6/\pi)\Bigg[2\,\sin\Phi\,\arccos\left(\tfrac{1+\cos\Phi}{-2\cos\Phi}\right)^{1/2} - (1-\cos\Phi)\,\arccos\tfrac{1+\cos\Phi}{-2\cos\Phi}\Bigg]\Bigg\} \quad \text{for} \quad \Phi_S \le \Phi \le \tfrac{2\pi}{3}, \quad (13)$$

where

$$\Phi_S \;=\; 2\arccos\left(3^{-1/2}\right) \;=\; \arccos\left(-\frac{1}{3}\right) \;\approx\; 109.47^\circ \quad (14)$$

This angle is called the *isogonal* angle in 3-D (Lévy-Leblond, 2004): the angle between lines connecting the centre of a regular tetrahedron with each of its vertices.

For the cumulative function we obtain

$$F(\Phi) \;=\; (4/\pi)(\Phi - \sin\Phi) \quad \text{for} \quad 0 \le \Phi \le \pi/2; \quad (15)$$

and

$$F(\Phi) \;=\; (4/\pi)\left[2\sin\Phi - 3\cos\Phi - 2\Phi + \tfrac{3\pi}{2} - 3\right] \quad \text{for} \quad \pi/2 \le \Phi \le \Phi_S; \quad (16)$$

For $\Phi_S \le \Phi \le \frac{2\pi}{3}$ we compute $F(\Phi)$ by numerical integration of (13).

3.2. Earthquake fault rotation

The naive way to simulate a random distribution is to select the strike, dip, and rake of a fault plane randomly

$$\phi \;=\; 360^\circ \times R_1\,, \quad (17)$$

$$\delta \;=\; 90^\circ \times R_2\,, \quad (18)$$

and

$$\lambda \;=\; 360^\circ \times R_3 - 180^\circ\,, \quad (19)$$

where R_i are selected as uniformly random variables in the interval $[0,1]$.

To check whether such a distribution is truly random, we may determine a 3-D angle of rotation or disorientation of a DC source compared to any given DC (Kagan, 1991). In particular, we determine the rotation angle starting with the strike-slip DC (Eqs. 5–7).

In Fig. 1, we display a 3-D rotation angle for two different random simulations. The naive approach (dashed line) produces a distribution incompatible with the theoretical random distribution (Eqs. 11–13): there are too many large rotations with the angle Φ close to 90°. This happens because for small dip angles, the rotations of the strike and rake angles are almost equivalent; hence too many among synthetic DCs have a small dip angle. This explains why Fig. 1 shows an excess of large 3-D rotation angles: the reference DC (Eqs. 5–7) has $\delta = 90^\circ$; therefore a simulated DC with δ close to zero requires that the rotation close to 90° coincide with the reference DC (5).

The proper method to calculate the random dip angle is by using a cosine transformation

$$\delta = \arccos R_2\,, \quad (20)$$

rather than selecting the uniformly random dip angle (18). The result of this simulation is shown in Fig. 1 and coincides with the theoretical curve.

We also checked whether the position of the rotation axis is distributed randomly over a 2-D sphere. It is not random for the first method of dip angle simulation (18), but it is uniformly random for the cosine transformation of the dip angle (20).

3.3. Eigenvector rotation

Several methods work for random rotation of eigenvectors (T-, P-, and B-axes). For example, we can select a random point on the surface of a 2-D (regular) sphere and use an axis through this point (pointing down). Another axis can be selected randomly in a plane orthogonal to the first, and a third axis orthogonal to the first two.

It is also possible to rotate a standard system of coordinates using the random orthogonal matrix described by Kendall & Moran (1963, Chapter 4.29). Again, the directions of the axes should be downward.

Perhaps the simplest technique is proposed by Frohlich (2001): select a random point on a sphere octant with its coordinates corresponding to sines of plunge angles (z_T, z_P, and z_B) for three axes (see Eq. 24). To simulate a random distribution of points on the surface of an octant, we first create a stochastic pattern of points on the surface of a sphere, using Marsaglia's (1972) algorithm. We then take the absolute values of synthetic coordinates. The plunge angles are

$$\alpha_T \;=\; \arcsin z_T\,, \quad (21)$$

and similarly for all other axes.

The azimuth of one axis (T-axis, for example) is selected randomly in the interval $0^\circ \le \beta_T < 360^\circ$. The azimuths for other axes can be calculated using the condition of axes orthogonality:

$$\beta_P \;=\; \beta_T + \arccos[-\tan\alpha_T \tan\alpha_P]\,, \quad (22)$$

similarly

$$\beta_B \;=\; \beta_T - \arccos[-\tan\alpha_T \tan\alpha_B]\,. \quad (23)$$

3.4. Quaternion rotation

To achieve quaternion random rotation, we use Marsaglia's (1972) method to generate a random point on the surface of a 3-D sphere in a 4-D space, and then interpret it as randomized rotation quaternion (Kagan, 1990; 1991; 1992b). The quaternion then is adjusted to represent a DC source (see Section 2.3). Other representations of DC source can be calculated if needed (Kagan, 1991, see FORTRAN programs in http://scec.ess.ucla.edu/~ykagan/dcrot_index.html).

4. Focal mechanism displays

4.1. Eigenvectors display

Frohlich (1992; 2001) remarks that three plunge angles satisfy the relation

$$\sin^2\delta_T + \sin^2\delta_P + \sin^2\delta_B \;=\; 1\,. \qquad (24)$$

Since all angles are positive, the above equation describes an octant of a sphere of the unit radius. Thus, the dip angle

$$\delta_S \;=\; \arcsin\frac{1}{\sqrt{3}} \;=\; \arctan\frac{1}{\sqrt{2}} \;\approx\; 35.26^\circ\,, \qquad (25)$$

is a symmetry point of a sphere octant: the equal angle between the symmetry line and the orthogonal planes of a coordinate system in 3-D.

Displaying the surface of a sphere on a flat surface has long occupied cartographers and astronomers. The major problem is that a sphere is not a *developable* surface (Snyder, 1993, p. 2): it cannot be laid flat without distortion. Many methods to address this challenge have been proposed over the last 2000 years (Snyder, 1993). Reignier (1957), Richardus and Adler (1972), and Bugayevskiy & Snyder (1995) discuss mathematical aspects of the problem. Geographical maps of globe octants go back to Leonardo da Vinci (Snyder, 1993, p. 40); Ward (1943) published an octant world map using equal-area projection.

Frohlich (1992) proposed displaying focal mechanisms using gnomonic projection of a sphere octant on an equilateral triangle. Later Frohlich (2001) indicated that this projection substantially distorts the area of a spherical surface, a distortion which may inhibit the study of focal mechanism distribution. He proposed another possible projection method to alleviate the problem.

Kaverina *et al.* (1996) proposed an equal-area projection: if $z_T = \sin\delta_T$, $z_P = \sin\delta_P$, and $z_B = \sin\delta_B$, then the equal-area projection of a sphere octant can be obtained as follows. We compute the length of the vector connecting the centre of the display with the projection point

$$L = 2\sin\left[\frac{1}{2}\arccos\frac{z_T + z_P + z_B}{\sqrt{3}}\right]\,, \qquad (26)$$

and the normalisation factor

$$N = \sqrt{2\left[(z_B - z_P)^2 + (z_B - z_T)^2 + (z_T - z_P)^2\right]}\,. \qquad (27)$$

The coordinates of a point in a triangle are

$$X = \frac{L}{N}\left(2z_B - z_P - z_T\right)\,, \qquad (28)$$

$$Y = \frac{L}{N}\left(z_T - z_P\right)\,. \qquad (29)$$

The areas where thrust, normal, and strike-slip mechanisms reside are separated by three lines which start at the [0, 0] point. The ends of the lines are: $[\sqrt{3}\,Y_S/2,\, Y_S/2]$, $[0,\, -Y_S]$, and $[-\sqrt{3}\,Y_S/2,\, Y_S/2]$, where

$$Y_S \;=\; 2\sin\left[\tfrac{1}{2}\arccos\sqrt{2/3}\right] \;=\; 2\sin\left[\delta_S/2\right]$$
$$=\; \sqrt{2\left(1-\sqrt{2/3}\right)} \;\approx\; 0.606\,. \qquad (30)$$

An example of the display is shown in Fig. 2.

4.2. Geologic fault parameters display

Both nodal planes are separated in the (δ,λ) diagrams by functions (solid line in Fig. 3)

$$\delta_\ell \;=\; 90^\circ \pm \arctan(\sin\lambda)\,. \qquad (31)$$

To illustrate the relationships between the two nodal planes in Fig. 3 we show several rectangles in the second nodal plane display and their image in the first plane, calculated according to Eqs. (1–3). Although the number of events in each polygon is the same, the images are rotated and their area significantly increases in the lower plot.

For the $[(1-\cos\delta),\lambda]$ or $[z,\lambda]$ plots

$$z_\ell \;=\; 1 \pm \frac{\sin\lambda}{\sqrt{1+\sin^2\lambda}}\,. \qquad (32)$$

Thrust/normal focal mechanisms are separated in the (δ,λ) diagram by vertical lines (shown as solid lines in Fig. 3), going from $\delta = 0^\circ$ to $\delta_S = 35.26^\circ$ for $\lambda = 0^\circ$ and $\pm 180^\circ$. Thrust/normal focal mechanisms are separated from strike-slip mechanisms by the following lines (also shown as dashed lines in Figs. 3)

$$\delta' \;=\; \arctan\tfrac{1}{\sqrt{2}\cos\lambda - \sin\lambda}$$
$$\text{for}\quad 0^\circ \le \lambda < \lambda_S \;=\; \arctan\sqrt{2}$$
$$=\; \arccos\left(3^{-1/2}\right) \;\approx\; 54.74^\circ\,, \qquad (33)$$

i.e.,

$$\lambda_S \;=\; 90^\circ \;-\; \delta_S\,, \qquad (34)$$

(see Eq. 25). For other branches of the separation line the abscissa values need to be reflected at zero or at 180°, or shifted to −180° (cf. Fig. 5).

The rake angle $\lambda_S \approx 54.74^\circ$ is an *equi-axial* angle in 3-D (Lévy-Leblond, 2004): the equal acute angle between a line and orthogonal axes. As Lévy-Leblond (2004) remarks, in 3-D

$$\lambda_S = \Phi_S/2\,, \qquad (35)$$

(see Eq. 14). Hence, all the symmetry angles Φ_S, δ_S, and λ_S are connected by simple relations (34) and (35).

Thrust/normal focal mechanisms are separated in the $[z,\lambda]$ plots by vertical lines (shown as solid lines in Fig. 4 and by dashed lines in Fig. 5), going from $z = 0$ to $z = 1 - \sqrt{2/3} \approx 0.184$. Thrust/normal focal mechanisms are separated from strike-slip mechanisms by the following lines (also shown as dashed lines in Figs. 4, 5)

$$z' \;=\; 1 - \sqrt{\tfrac{1}{1+(\sqrt{2}\cos\lambda - \sin\lambda)^{-2}}}$$
$$\text{for}\quad 0^\circ \le \lambda < \lambda_S\;(54.74^\circ)\,. \qquad (36)$$

The abscissa for other branches of the separation line follows the same rule as (33).

As in Fig. 3 we show several rectangles in the second nodal plane display and their image in the first plane, calculated according to Eqs. (1–3). The images are rotated but their area remains the same in the lower plot. This feature is to be expected since the cosine transformation of the dip angle (δ) is area preserving. Calculating the integral for z_ℓ we obtain

$$\int_0^\pi \frac{\sin\lambda}{\sqrt{1+\sin^2\lambda}}\,d\lambda \;=\; \pi/2\,, \qquad (37)$$

i.e., each nodal plane occupies one-half of the $[(1-\cos\delta),\lambda]$ plane rectangle.

The advantage of the display in Figs. 3 and 4 is that the full plot is a cylinder (see also Fig. 5 description below) or *developable* surface. That is it can be laid flat without distortion. However, the drawback is that each earthquake is plotted twice on a diagram. In many types of analysis we would need to distinguish a fault from an auxiliary plane, a task not easy to perform.

4.3. Quaternion display

The quaternion DC representation does not submit itself to easy visualization, but for completeness sake we briefly consider how one can display focal mechanisms given their quaternion characterization. The general normalized quaternion

$$\mathbf{q} = [q_1, q_2, q_3, q_4], \tag{38}$$

can be rotated around a vertical axis into a position with $q_3 = 0$. To accomplish this we use a quaternion

$$\mathbf{p} = [0, 0, p_3, p_4], \tag{39}$$

where $p_3 = q_3/\sqrt{q_3^2 + q_4^2}$ and $p_4 = q_4/\sqrt{q_3^2 + q_4^2}$. Then the rotated quaternion is obtained as in (10).

$$\mathbf{s} = \mathbf{pq}. \tag{40}$$

The quaternion $\mathbf{s}$ has 3 components ($\mathbf{s} = [s_1, s_2, 0, s_4]$), but since it is normalized, it has only 2 free parameters. These 2 degrees of freedom correspond to a 2-D sphere. Thus, we have the old problem (see Section 4.1) of displaying a spherical surface on a flat 2-D space. Because of our quaternion parametrization (Section 2.3), we must convert the quaternion space to an octant similar to that in Section 3.3. We calculate

$$\begin{aligned} \sin\delta_T &= |\sin[2\arccos(s_4)]| \times \left[1 + (s_1^2/s_2^2)\right]^{-1/2}|, \\ \sin\delta_P &= |(s_1/s_2)\sin[2\arccos(s_4)]| \times \left[1 + (s_1^2/s_2^2)\right]^{-1/2}|, \\ \sin\delta_B &= |2s_4^2 - 1|. \end{aligned} \tag{41}$$

Thereafter, the display can be carried out as in Section 4.1.

5. Discussion

How can we use the methods discussed in this paper? Sets of randomly rotated DC sources can be produced by any of the techniques proposed here. If needed, any variable in the simulations can be restricted to a certain interval, and as a result, the rotation distribution would be uniform inside the new smaller restricted domain.

The displays of focal mechanisms can be used to investigate deformation patterns in seismogenic zones. For example, Frohlich (2001), Kagan (2000), Huc & Main (2003) did so when investigating aspects of focal mechanism statistical distributions.

As an example of such displays, Figs. 5 and 6 show a set of focal mechanisms of earthquakes occurring on the ocean side of subduction zones (Bird & Kagan, 2004). In Fig. 5 the left boundary of the plot is identical to the right; hence, the diagram can be considered a surface of a cylinder (see the last paragraph of Subsection 4.2). Most focal mechanisms are either thrust or normal type. Since they are shown on the area-preserving maps, their distribution can be studied without any bias from probability density distortions (Frohlich, 2001).

How can the distributions of focal mechanisms be studied in these displays? Frohlich (2001) proposes dividing the gnomonic triangular display into equilateral sub-triangles to separate mechanisms into a discrete number of cells. These discrete arrays would be of value for statistical comparisons with a model or some other set of mechanisms.

One disadvantage of the triangular subdivision is that triangles have a large diameter (length of a side) compared to their area. In many applications it is preferable that comparison cells be as close to a circle as possible. A second drawback is that these triangles are not easy to visualize without a computer.

In contrast, Saff & Kuijlaars (1997) propose equal-area sphere partition which uses rectangular, square-like cells. Since these cells have parallels and meridians as their boundaries, they are easier to visualize. Kagan & Jackson (1998, their Fig. 3) apply a similar subdivision to a sphere octant. The number of focal mechanisms in each triangular or rectangular spherical cell can again be compared against other distributions. However, in an octant partition, one corner is included in a spherical triangle, whereas rectangular cells contain two triangle corners. Therefore, one of the eigenvectors has a distinctive role in the subdivision, a feature which may hinder statistical analysis.

It is perhaps more difficult to find a partition for geologic/tectonic displays (Figs. 3, 4, and 5). For example, the dip angle may change within one tectonic province so that its distribution straddles the boundary between two nodal planes, as we see in Fig. 5 for normal earthquakes. However, the distribution of thrust earthquakes in Fig. 5 exhibits evident separation which can be used for statistically select the fault plane. Methods statistical analysis of these displays need to be explored and developed.

6. Conclusions

- We discussed four representations for a DC earthquake source: eigenvector, tectonic, seismic moment, and quaternion. These expressions are mathematically equivalent, but each has certain advantages and drawbacks.
- Random 3-D rotation of a DC source is often needed for statistical tests. This rotation presents a more difficult problem than a 2-D rotation. Some seemingly obvious techniques for rotating any object and a DC source especially produce an erroneous result. We provide formulae for a 3-D random rotation for all four representations of a DC source.
- We discussed requirements for displaying earthquake focal mechanisms. Two displays – one based on eigenvector and the other based on geologic/tectonic representation – may be useful to analyze focal mechanism distributions in various tectonic provinces.

Acknowledgments. I appreciate partial support from the National Science Foundation through grants EAR 00-01128, EAR 04-09890, DMS-0306526, from CalTrans grant 59A0363, and from the Southern California Earthquake Center (SCEC). SCEC is funded by NSF Cooperative Agreement EAR-0106924 and USGS Cooperative Agreement 02HQAG0008. I thank C. Frohlich (University of Texas), H. Houston and P. Bird of UCLA for very useful remarks and discussions. Comments by C. Frohlich and an anonymous reviewer have been helpful in revision of the manuscript. Kathleen Jackson edited the final version. Publication 876, SCEC.

References

Aki, K. & P. Richards, 2002. *Quantitative Seismology*, 2nd ed., Sausalito, Calif., University Science Books, 700 pp.

Ben-Menahem, A. & Singh, S. J., 1981. *Seismic Waves and Sources*, Springer-Verlag, NY, pp. 1108.

Bird, P., & Y. Y. Kagan, 2004. Plate-tectonic analysis of shallow seismicity: apparent boundary width, beta, corner magnitude, coupled lithosphere thickness, and coupling in seven tectonic settings, *Bull. Seismol. Soc. Amer.*, **94**(6), 2380-2399.

Bugayevskiy, L. M., & J. P. Snyder, 1995. *Map Projections: A Reference Manual*, Taylor & Francis, London, pp. 328.

Dziewonski, A. M. & Woodhouse, J. H., 1983. Studies of the seismic source using normal-mode theory, in: *Earthquakes: Observation, Theory and Interpretation*, Proc. Int. School Phys. "Enrico Fermi", Course LXXXV, eds H. Kanamori & E. Boschi, North-Holland Publ., Amsterdam, 45-137.

Ekström, G., A. M. Dziewonski, N. N. Maternovskaya & M. Nettles, 2005. Global seismicity of 2003: Centroid-moment-tensor solutions for 1087 earthquakes, *Phys. Earth Planet. Inter.*, **148**(2-4), 327-351.

Frohlich, C., 2001. Display and quantitative assessment of distributions of earthquake focal mechanisms, *Geophys. J. Int.*, **144**, 300-308.

Frohlich, C., 1996. Cliff's nodes concerning plotting nodal lines for P, S_h, and S_v, *Seismol. Res. Lett.*, **67**(1), 16-24.

Frohlich, C., 1992. Triangle diagrams: ternary graphs to display similarity and diversity of earthquake focal mechanisms, *Phys. Earth Planet. Inter.*, **75**, 193-198.

Frohlich, C., & S. D. Davis, 1999. How well constrained are well-constrained T, B, and P axes in moment tensor catalogs?, *J. Geophys. Res.*, **104**, 4901-4910.

Hardebeck, J. L., & P. M. Shearer, 2002. A new method for determining first-motion focal mechanisms, *Bull. Seismol. Soc. Amer.*, **92**(6), 2264-2276.

Huc, M., & I. G. Main, 2003. Anomalous stress diffusion in earthquake triggering: Correlation length, time dependence, and directionality, *J. Geophys. Res.*, **108**(B7), ESE-1, pp. 1-12, art. no. 2324.

Jost, M. L., & R. B. Herrmann, 1989. A student's guide to and review of moment tensors, *Seismol. Res. Lett.*, **60**(2), 37-57.

Kagan, Y. Y., 1982. Stochastic model of earthquake fault geometry, *Geophys. J. Roy. astr. Soc.*, **71**, 659-691.

Kagan, Y. Y., 1990. Random stress and earthquake statistics: Spatial dependence, *Geophys. J. Int.*, **102**, 573-583.

Kagan, Y. Y., 1991. 3-D rotation of double-couple earthquake sources, *Geophys. J. Int.*, **106**, 709-716.

Kagan, Y. Y., 1992a. On the geometry of an earthquake fault system, *Phys. Earth Planet. Inter.*, **71**(1-2), 15-35.

Kagan, Y. Y., 1992b. Correlations of earthquake focal mechanisms, *Geophys. J. Int.*, **110**, 305-320.

Kagan, Y. Y., 2000. Temporal correlations of earthquake focal mechanisms, *Geophys. J. Int.*, **143**, 881-897.

Kagan, Y. Y., & D. D. Jackson, 1994. Long-term probabilistic forecasting of earthquakes, *J. Geophys. Res.*, **99**, 13,685-13,700.

Kagan, Y. Y., & D. D. Jackson, 1998. Spatial aftershock distribution: Effect of normal stress, *J. Geophys. Res.*, **103**, 24,453-24,467.

Kagan, Y. Y., & L. Knopoff, 1985. The first-order statistical moment of the seismic moment tensor, *Geophys. J. Roy. astr. Soc.*, **81**, 429-444.

Kaverina, A. N., A. V. Lander, & A. G. Prozorov, 1996. Global creepex distribution and its relation to earthquake-source geometry and tectonic origin, *Geophys. J. Int.*, **125**, 249-265.

Kendall, M. G., & Moran, P. A. P., 1963. *Geometrical Probabilities*, Hafner, N. Y., 125 pp.

Kuipers, J. B., 2002. *Quaternions and Rotation Sequences: A Primer with Applications to Orbits, Aerospace and Virtual Reality*, Princeton, Princeton Univ. Press., 400 pp.

Le Pichon, X., J. Francheteau, & J. Bonnin, 1973. *Plate Tectonics*, Elsevier, London, pp. 300.

Lévy-Leblond, J.-M., 2004. N-dimensional variations on themes of Pythagoras, Euclid, and Archimedes, *Mathematical Intelligencer*, **26**(3), 43-53.

Marsaglia, G., 1972. Choosing a point from the surface of a sphere, *Ann. Math. Stat.*, **43**, 645-646.

Pujol, J., & R. B. Herrmann, 1990. A student's guide to point sources in homogeneous media, *Seismol. Res. Lett.*, **61**(3-4), 209-224.

Reignier, F., 1957. *Systèmes de projection et leurs applications à la géographie, à la cartographie, à la navigation, à la topométrie, etc.*, Vols. 1-2, Paris.

Richardus, P., & R. K. Adler, 1972. *Map projections for geodesists, cartographers and geographers*, Amsterdam, North-Holland Pub. Co., pp. 174.

Saff, E. B., & A. B. J. Kuijlaars, 1997. Distributing many points on a sphere, *Mathematical Intelligencer*, **19**, 5-11.

Snyder, J. P., 1993. *Flattening the Earth: Two Thousand Years of Map Projections*, Univ. Chicago Press, Chicago, 365 pp.

Steacy, S., D. Marsan, S. S. Nalbant, & J. McCloskey, 2004. Sensitivity of static stress calculations to the earthquake slip distribution, *J. Geophys. Res.*, **109**(B4), Art. No. B04303.

Ward, H. B., ed., 1943. *Octovue Map of the World*, Milwaukee, L. E. Pitner, pp. 20.

Ward, J. P., 1997. *Quaternions and Cayley Numbers: Algebra and Applications*, Kluwer Acad. Pub., London, pp. 237.

Yan Y. Kagan, Department of Earth and Space Sciences, University of California, Los Angeles, California, 90095-1567, USA; (e-mail: ykagan@ucla.edu)

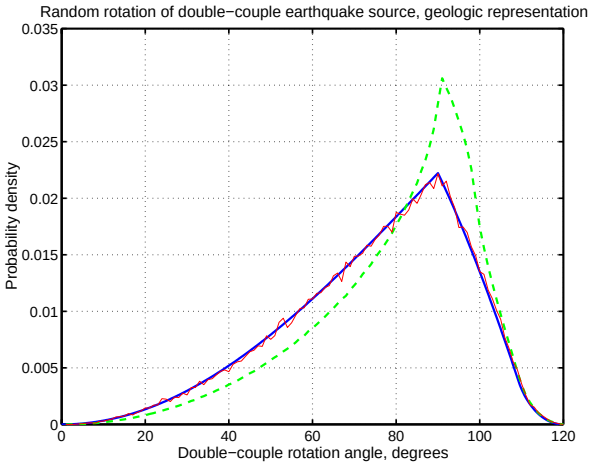

Figure 1. Distributions of rotation angles for DCs, geologic parametrization. Solid line represents theoretical DC random rotation (Eqs. 11–13), dashed line represents simulations (10^7 realizations) in which strike, dip, and rake are selected randomly (Eqs. 17–19). Thin solid line corresponds to the simulation with cosine transformation of the dip angle (Eq. 20). We simulated this distribution with a small number of events (10^5 realizations); otherwise the curve would coincide with the theoretical distribution.

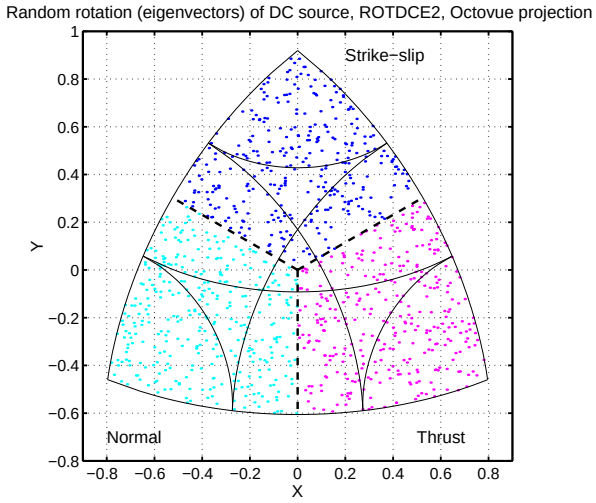

Figure 2. Focal mechanism display for DC eigenvector representation. 1000 DC random mechanisms are simulated and shown as points at octant equal-area projection. The DC distribution is uniform over the projection plane. Dashed lines are boundaries of strike-slip, normal, and thrust mechanisms. Plunge angles 30° and 60° for all mechanisms are shown by thin solid lines.

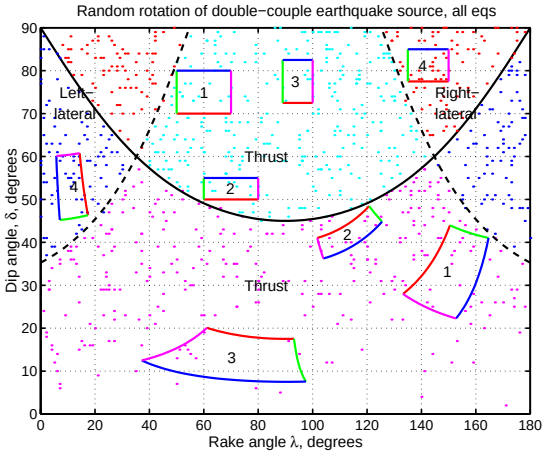

Figure 3. Focal mechanism display for DC geologic representation. 1000 DC random mechanisms are simulated and shown as points at (δ, λ) diagram. The diagram for negative rake ($0° \geq \lambda \geq -180°$) angle is analogous. Thrust events are replaced by earthquakes with a normal focal mechanisms for $0° \geq \lambda$. The distribution is not uniform along the δ-axis. Solid line separate two nodal planes, so that $\delta_2 \geq \delta_1$. Dashed lines are boundaries between strike-slip, normal, and thrust mechanisms. To illustrate interrelations between two nodal planes, several rectangles are selected in the second nodal plane and their transformations shown in the first. Note distortion in the area of each rectangle pair using this presentation.

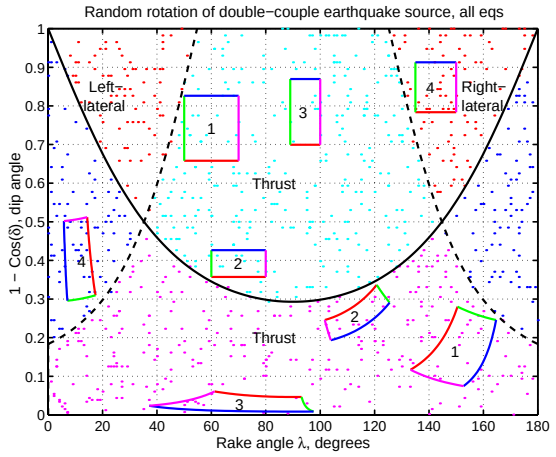

Figure 4. Focal mechanism display for DC geologic representation. 1000 DC random mechanisms are simulated and shown as points at $[(1-\cos\delta),\lambda]$ diagram. The diagram for negative rake ($0° \geq \lambda \geq -180°$) angle is analogous; thrust events are replaced by earthquakes with a normal focal mechanisms. The distribution is uniform over the plane. Solid line separate two nodal planes, so that $\delta_2 \geq \delta_1$. Dashed lines are boundaries between strike-slip, normal, and thrust mechanisms. To illustrate interrelations between two nodal planes, several rectangles – the same as in Fig. 3 – are selected in the second nodal plane and their transformations shown in the first. The transformed rectangles preserve their area, demonstrating the desired equal-area uniformity of the presentation. However, distances between various focal mechanism points may be significantly modified.

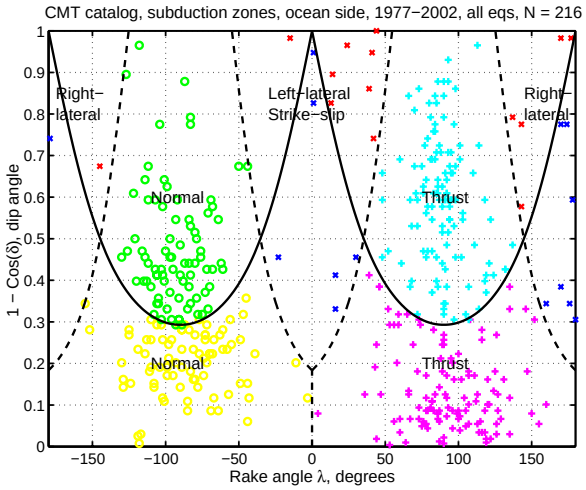

Figure 5. Focal mechanism display for DC geologic representation. Earthquakes on the ocean side of subduction zones are selected by Bird & Kagan (2004) from the Harvard catalogue of 1977-2002/9/30. The total number of earthquakes is 216. Each earthquake is displayed twice for both nodal planes; the relation between symbol positions of each event is illustrated in Fig. 4. Solid lines separate two nodal planes, so that $\delta_2 \geq \delta_1$. Dashed lines are boundaries of strike-slip, normal, and thrust mechanisms.

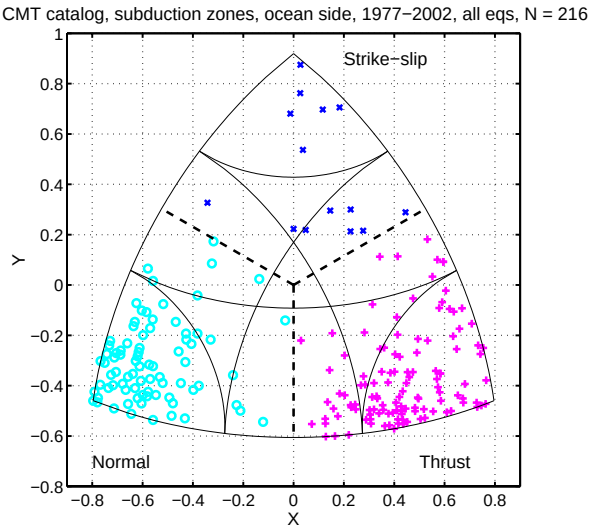

Figure 6. Focal mechanism display for DC eigenvector representation. Earthquakes on the ocean side of subduction zones are selected by Bird & Kagan (2004) from the Harvard catalogue of 1977-2002/9/30. Focal mechanisms are shown as symbols at octant equal-area projection (Eqs. 28–29). The total number of earthquakes is 216. As in Fig. 2 dashed lines are boundaries of strike-slip, normal, and thrust mechanisms. Plunge angles 30° and 60° for all mechanisms are shown by thin solid lines.